How to cite: *Angew. Chem. Int. Ed.* **2022,** *61,* e202204108
International Edition: doi.org/10.1002/anie.202204108
German Edition: doi.org/10.1002/ange.202204108

MOF-Based Photocatalysts

Charge Separation by Creating Band Bending in Metal–Organic Frameworks for Improved Photocatalytic Hydrogen Evolution

*Chenxi Zhang, Chenfan Xie, Yuying Gao, Xiaoping Tao, Chunmei Ding, Fengtao Fan, and Hai-Long Jiang**

Abstract: Metal–organic frameworks (MOFs) have been intensively studied as a class of semiconductor-like materials in photocatalysis. However, band bending, which plays a crucial role in semiconductor photocatalysis, has not yet been demonstrated in MOF photocatalysts. Herein, a representative MOF, MIL-125-NH_2, is integrated with the metal oxides (MoO_3 and V_2O_5) that feature appropriate work functions and energy levels to afford the corresponding MOF composites. Surface photovoltage results demonstrate band bending in the MOF composites, which gives rise to the built-in electric field of MIL-125-NH_2, boosting the charge separation. As a result, the MOF composites present 56 and 42 times higher activities, respectively, compared to the pristine MOF for photocatalytic H_2 production. Upon depositing Pt onto the MOF, ~6 times higher activity is achieved. This work illustrates band bending of MOFs for the first time, supporting their semiconductor-like nature, which would greatly promote MOF photocatalysis.

Introduction

Solar energy can be converted into chemical energy by photocatalytic processes, which is considered a promising solution to the current energy crisis and environmental pollution issues.[1] However, the poor separation efficiency of photogenerated carriers poses a significant challenge toward the further development of photocatalysis.[2] Various strategies have been developed to meet this challenge, including the common approaches, for example, the construction of a heterojunction[3] or Z-/S-scheme,[4] the formation of defects,[5] introduction of cocatalyst,[6] and crystal facet engineering.[7] In addition, on the prerequisite of possessing appropriate work functions and energy levels, some metal oxides are able to act as the regulator to tune the Fermi level and the conductive/valence band level of semiconductor photocatalysts. Accordingly, the electrons can be injected into or extracted from the semiconductor to generate band bending. The resulting charge imbalance leads to the built-in electric field, which is crucial to suppress the recombination of the photogenerated carriers.[8] Very recently, Tao et al. observed upward band bending and an intensive built-in electric field at the surface of Bi_4TaO_8X (X = Cl, Br) upon decorating MoO_3 or V_2O_5. The decorated Bi_4TaO_8X (X = Cl, Br) gave significantly improved photocatalytic oxygen production activity, and the apparent quantum efficiency (AQE) of the catalyst exceeded 25 % at 420 nm,[9] suggesting that the introduction of suitable metal oxides is able to regulate the charge properties of the semiconductor photocatalysts for enhanced activity.

In recent years, a class of porous crystalline solids, metal–organic frameworks (MOFs), have been intensively studied for photocatalysis, given their well-defined and tunable structures, high porosity, large surface area, and so on.[10] To improve their charge separation, MOFs are integrated with different functional materials to form composite photocatalysts.[11] Despite band bending alike mechanism has possibly been adopted to explain the enhanced charge separation and activity for MOFs,[12] unfortunately, to the best of our knowledge, band bending has never been demonstrated in MOF-based materials yet. It remains a controversial issue on considering MOFs as molecular photocatalysts or semiconductor-like photocatalysts thus far.[13] The evidence on band bending in MOFs is of great significance to understand the mechanism in enhanced photocatalysis over MOF-based composites.

With the above considerations in mind, a representative MOF, namely MIL-125-NH_2,[6f,14] was adopted to be integrated with metal oxides MoO_3 and V_2O_5, respectively affording MoO_3/MIL-125-NH_2 and V_2O_5/MIL-125-NH_2. Band bending as well as the built-in electric field of MIL-125-NH_2 is identified by surface photovoltage (SPV) spectra and solid-state current–voltage (*I–V*) curves, respectively. As a result, MoO_3/MIL-125-NH_2 and V_2O_5/MIL-125-NH_2 give much increased activities, which are 56 and 42 times higher than the pristine MOF, respectively, reaching 399.0 and 298.6 $\mu mol\,g^{-1}\,h^{-1}$, in the photocatalytic H_2 production

[*] Dr. C. Zhang, C. Xie, Prof. Dr. H.-L. Jiang
Department of Chemistry,
University of Science and Technology of China
Hefei, Anhui 230026 (P. R. China)
E-mail: jianglab@ustc.edu.cn
Homepage: http://staff.ustc.edu.cn/~jianglab/
Dr. Y. Gao, Dr. C. Ding, Prof. Dr. F. Fan
State Key Laboratory of Catalysis, Dalian National Laboratory for Clean Energy, Dalian Institute of Chemical Physics,
Chinese Academy of Sciences
Dalian, Liaoning 116023 (P. R. China)
Dr. X. Tao
Research Initiative for Supra-Materials, Interdisciplinary Cluster for Cutting Edge Research, Shinshu University
Nagano, 380-8553 (Japan)

by water splitting (Scheme 1). In addition, when deliberately depositing Pt cocatalyst onto diverse locations, the catalyst with Pt on the MOF exhibits the highest activity, suggesting that the MOF generates electrons and then migrates to Pt sites, where proton reduction takes place. As far as we know, this is the first report on clarifying the band bending in MOFs, which reflects their semiconductor-like nature.

Results and Discussion

MIL-125-NH_2 was synthesized by a traditional solvothermal method.[15] The MoO_3 particles were obtained by treating $(NH_4)_6Mo_7O_{14}{\cdot}4H_2O$ at 350 °C for 2 h in air with the heating rate of 1 °C min^{-1}, and the commercial V_2O_5 was ball-milled to reduce its particle sizes. The metal oxides were integrated with the MOF by an impregnation method to afford MoO_3/MIL-125-NH_2 and V_2O_5/MIL-125-NH_2 composites, respectively (see Supporting Information, Experimental Section).

Powder X-ray diffraction (XRD) patterns for the MOF composites display the characteristic peaks of MIL-125-NH_2, demonstrating its good crystallinity (Figure S1). Scanning electron microscope (SEM) images give the morphology information for the metal oxides and composites (Figure S2a, b). It can be observed that the metal oxide particles are loaded on the MOF surface. The average sizes of MoO_3 and V_2O_5 are 458.9 ± 388.0 and 77.6 ± 17.8 nm, respectively (Figure S2c, d, S3), which are roughly the same as those of metal oxide particles on the MOF (Figure S2a, b). High-resolution transmission electron microscope (HRTEM) observation for MoO_3/MIL-125-NH_2 and V_2O_5/MIL-125-NH_2 indicates the interplanar distances of MoO_3 and V_2O_5 are 0.327 and 0.437 nm, corresponding to the lattice spacing of (021) of MoO_3 and (001) of V_2O_5, respectively (Figure 1a, b). Given the low contents of metal oxides (5.0 wt % for both MoO_3 and V_2O_5) in the composites, it is difficult to identify their peaks in the powder XRD patterns. Alternatively, Raman spectra have been conducted to prove the presence of the metal oxides (Figure 1c). Compared with the pristine MOF, the new peaks of MoO_3/MIL-125-NH_2 and V_2O_5/MIL-125-NH_2 exactly correspond to the characteristic peaks of the metal oxides, indicating the successful integration.

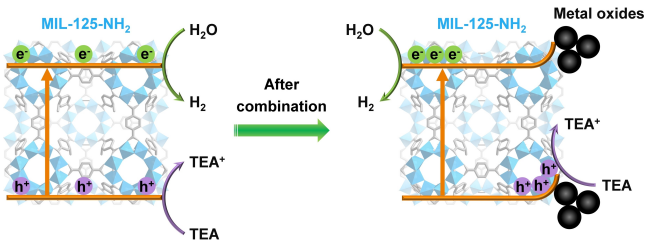

Scheme 1. Schematic diagram of photocatalytic H_2 production over MIL-125-NH_2 before and after the integration with the metal oxides.

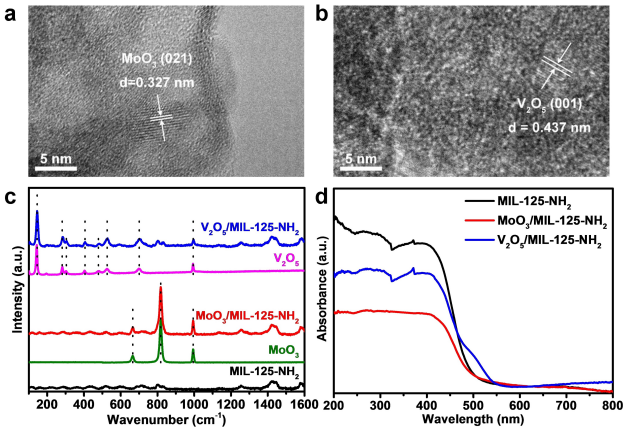

Figure 1. HRTEM images of a) MoO_3/MIL-125-NH_2 and b) V_2O_5/MIL-125-NH_2. c) Raman spectra of MIL-125-NH_2, MoO_3, MoO_3/MIL-125-NH_2, V_2O_5, and V_2O_5/MIL-125-NH_2. d) DR UV/Vis spectra of MIL-125-NH_2, MoO_3/MIL-125-NH_2, and V_2O_5/MIL-125-NH_2.

Nitrogen-sorption profiles of MIL-125-NH_2, MoO_3/MIL-125-NH_2, and V_2O_5/MIL-125-NH_2 are similar (Figure S4). Their Brunauer–Emmett–Teller (BET) surface areas are 847, 837, and 782 $m^2 g^{-1}$, respectively, where the slight decrease of surface area in the composites would be ascribed to the mass contribution by metal oxides. The ultraviolet-visible (DR UV/Vis) absorption spectra give similar results while the absorption intensity slightly decreases in the composites (Figure 1d), which is attributed to the poor light absorption performance and large band gaps of the metal oxides (Figure S5). No obvious change in color can be seen for all three samples (Figure S6). The calculated band gap of MIL-125-NH_2 is 2.65 eV (Figure S7a). Along with the Mott–Schottky plots, the energy level of MIL-125-NH_2 can be determined (Figure S7b). The lowest unoccupied molecular orbital (LUMO) level of MIL-125-NH_2 is −0.60 V vs. NHE, which is more negative than the H^+/H_2 redox potential (0.00 V vs. NHE), indicating the potential of MIL-125-NH_2 in the photocatalytic H_2 production. The highest occupied molecular orbital (HOMO) level of MIL-125-NH_2 is +2.05 V vs. NHE, which is more negative than the conduction band (CB) of MoO_3 and V_2O_5.[16] The results convince the feasibility of electrons spontaneously migrating from the MOF to the metal oxides in terms of thermodynamics, giving rise to the upward band bending at the surface of MIL-125-NH_2 (Scheme 2).

To determine the surface work functions of MIL-125-NH_2, MoO_3, and V_2O_5, the surface potentials have been measured by the Kelvin probe force microscope (KPFM). The surface potential of MIL-125-NH_2 is ca. 200 and 300 mV higher than those of MoO_3 and V_2O_5, representing the more negative Fermi level of MIL-125-NH_2 (Figure 2a). This indicates that, once they are closely contacted, the electrons would migrate from the MOF to the metal oxides spontaneously in terms of thermodynamics, which results in the different static potentials in the MOF and gives rise to upward band bending. Meanwhile, the electron transfer in MIL-125-NH_2 leaves positively charged species at the surface, creating the built-in electric field close to the MOF surface. According to the X-ray photoelectron spectroscopy (XPS) spectra, Mo and V elements in the composites are in +6 and +5 valence, respectively, reflecting that they are in

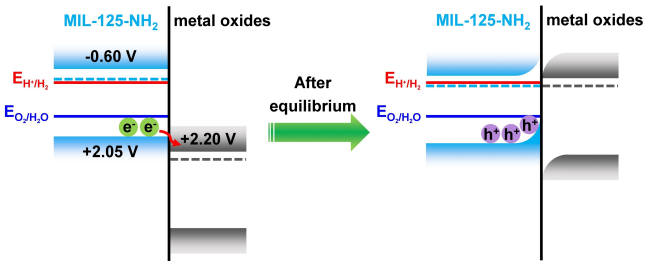

Scheme 2. Schematic mechanism for the band bending and built-in electric field formation, as well as related energy levels of both components in the MOF composites. The dash lines represent the Fermi levels of the MOF and metal oxides. The red and blue solid lines represent the energy potentials for H^+/H_2 and O_2/H_2O (0.00 and 1.23 V vs. NHE), respectively. Upon loading the metal oxides, the LUMO level of MIL-125-NH_2 may positively shift, but not become positive, due to the much larger MOF particle sizes than the metal oxides.

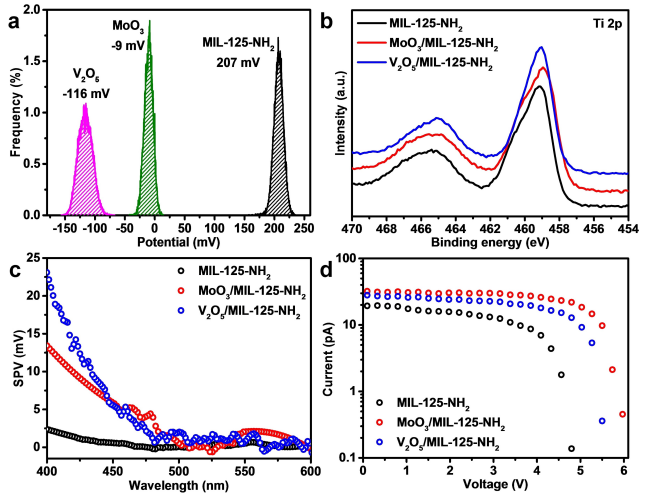

Figure 2. a) Surface potentials of MIL-125-NH_2, MoO_3, and V_2O_5. b) Ti 2p XPS spectra, c) SPV spectra, and d) *I–V* curves of MIL-125-NH_2, MoO_3/MIL-125-NH_2, and V_2O_5/MIL-125-NH_2.

the common oxidation states (Figure S8). Moreover, when integrating with these metal oxides, the Ti binding energy of MIL-125-NH_2 presents a negative shift, which should be caused by the electron transfer from the MOF to the metal oxides, indirectly proving the occurrence of band bending in the MOF (Figure 2b).[17] To further gain direct evidence of upward band bending, the SPV spectra have been collected. Compared to MIL-125-NH_2, the MoO_3/MIL-125-NH_2 and V_2O_5/MIL-125-NH_2 composites show significantly stronger SPV signals, demonstrating the increment of the hole accumulation concentration on the surface of the MOF (Figure 2c).[18] The result unambiguously demonstrates that band bending does occur to the MOF upon its integration with the oxides.[19] In the solid-state current–voltage (*I–V*) curves, the currents of MoO_3/MIL-125-NH_2 and V_2O_5/MIL-125-NH_2 are higher than that of sole MIL-125-NH_2, and the inflection point potentials of the formers are more positive than that of the latter, inferring that the higher energy is necessary for electrons passing through the interface region in the composites (Figure 2d, S9). In other words, the built-in electric field formed in MIL-125-NH_2, upon the integration with the metal oxides, facilitates the charge separation of the MOF.

Photoelectrochemical (PEC) measurements have been carried out for MIL-125-NH_2, MoO_3/MIL-125-NH_2, and V_2O_5/MIL-125-NH_2. The photocurrent densities of the MOF composites are higher than that of the pristine MIL-125-NH_2 (Figure 3a), indicating enhanced separation of photogenerated carriers in the composites, which exactly presents the same trend of intensity difference of steady-state photoluminescence (PL) emission spectra (Figure 3b). According to the electrochemical impedance spectroscopy (EIS) Nyquist plots and the fitting results, the series resistances (Rs) of all the samples are comparable, whereas the charge transfer resistances (R_{ct}) of the composites are much smaller than that of the MOF (Figure 3c, S10a, and Table S1). These samples demonstrate similar curves in both low-frequency and high-frequency regions of EIS Bode plots, supporting that they follow the same charge transfer path (Figure S10b). The results reveal that the charge transfer process gets accelerated in the composites. The average photogenerated carrier lifetimes (τ_n) are measured by the open circuit voltage decay (OCVD) method (Figure 3d, S11). The catalysts MoO_3/MIL-125-NH_2 and V_2O_5/MIL-125-NH_2 show obviously longer τ_n than the pristine MIL-125-NH_2, indicating their lower recombination rate of charge carriers. To quantitatively determine the surface charge injection efficiency ($\eta_{surface}$) and bulk charge separation efficiency (η_{bulk}), 0.5 mol L^{-1} of H_2O_2 is added in the electrolyte as the hole scavenger. Both $\eta_{surface}$ and η_{bulk} at 1.23 V vs. RHE of MoO_3/MIL-125-NH_2 (78.0 % and 29.7 %) and V_2O_5/MIL-125-NH_2 (75.4 % and 28.2 %) are higher than those of MIL-125-NH_2 (70.0 % and 25.9 %), representing the significant influence of band bending on improving charge separation efficiency (Figure S12). All above results consistently support that the

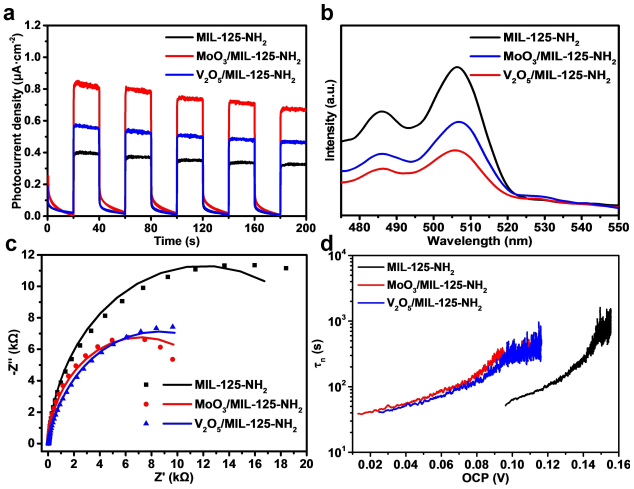

Figure 3. a) Photocurrent responses, b) PL spectra under excitation at 380 nm, c) EIS Nyquist plots, and d) average lifetime of the photogenerated carriers (τ_n) of MIL-125-NH_2, MoO_3/MIL-125-NH_2, and V_2O_5/MIL-125-NH_2 obtained from the OCVD curves.

presence of band bending in the MOF upon integration with the oxides leads to the built-in electric field and enhanced charge separation.

Encouraged by the above characterizations, we then set out to investigate photocatalytic H_2 production by water splitting under visible light irradiation. For photocatalysis over MIL-125-NH_2, the amino-modified linker as an antenna would be photoexcited by visible light to migrate electrons to the Ti-oxo clusters. Given its weak charge separation capability, the pristine MIL-125-NH_2 displays poor activity (7.1 $\mu mol\,g^{-1}\,h^{-1}$). Despite its negligible activity, its color changes from gray to blue under light irradiation,[20] indicating that Ti^{4+} is reduced to Ti^{3+} in the MOF and the Ti-oxo clusters are able to be adopted for proton reduction. Significantly, MoO_3/MIL-125-NH_2 and V_2O_5/MIL-125-NH_2 show remarkable H_2 production rates of 399.0 and 298.6 $\mu mol\,g^{-1}\,h^{-1}$, around 56 and 42 times higher than the pristine MOF (Figure 4a, S13), revealing that the band bending of the MOF evoked by the metal oxides plays a critical role in boosting its catalytic activity. The AQEs of the composites are evaluated under light irradiation at 380 nm (Table S2). Compared to those under visible light irradiation, the activities of both the MOF and its composites present negligible activity in the dark, hinting the real photocatalytic process, where the reactions are driven by the light absorption (Figure S14). Control experiments suggest that the close contact between MIL-125-NH_2 and the metal oxides is crucial to the enhanced activity. Compared with the MOF composites in which both components are in close contact, the physical mixtures of MoO_3&MIL-125-NH_2 and V_2O_5&MIL-125-NH_2 give much lower activity (Figure S15). In the physical mixtures, the loose contact between MOF and the metal oxides is detrimental to the mutual electron transfer, which cannot lead to the occurrence of band bending. These illustrate that the occurrence of band bending and built-in electric field to the MOF should be based on the premise of close contact between the MOF and metal oxides.

The influence on activity by the loading amount of the metal oxides onto the MOF manifests a volcano-type curve, in which 5.0 wt % of MoO_3 and V_2O_5 in the MOF composites show the highest photocatalytic activity (Figure S16, S17). It is assumed that excessive metal oxides may shield the MOF from light harvesting and block the active sites. The relationships between photocatalytic hydrogen production activities of the photocatalysts and the irradiation wavelengths, catalyst amounts, pH values, and scavenger concentrations have been investigated, figuring out the optimized reaction conditions (Figure S18). Moreover, no obvious decrease in the activity of MoO_3/MIL-125-NH_2 and V_2O_5/MIL-125-NH_2 can be observed during the five consecutive cycles (Figure 4b, S19). Their powder XRD patterns are also maintained after the recycling (Figure S20), indicating their good stability in the reaction.

To unveil the electron transfer path and the reaction site of H_2 production, Pt has been deposited as the cocatalyst onto different places, including the MOF (i.e., MO_x/(Pt/MIL-125-NH_2)), random locations (i.e., Pt/(MO_x/MIL-125-NH_2)), and the metal oxides (i.e., (Pt/MO_x)/MIL-125-NH_2), respectively (Scheme 3). The H_2 production rates of the catalysts with MoO_3 and V_2O_5 follow the same orders of MoO_3/(Pt/MIL-125-NH_2) > Pt/(MoO_3/MIL-125-NH_2) > (Pt/MoO_3)/MIL-125-NH_2 and V_2O_5/(Pt/MIL-125-NH_2) > Pt/(V_2O_5/MIL-125-NH_2) > (Pt/V_2O_5)/MIL-125-NH_2 under visible light irradiation (>380 nm) (Figure 4c,d, S21). In other words, the Pt location does matter the activity. The highest activity can be observed when Pt is deposited on the MOF where the photogenerated electrons should be originally accumulated. In Pt/(MO_x/MIL-125-NH_2), less Pt deposition amount on the MOF leads to less active sites and lower activity than those in MO_x/(Pt/MIL-125-NH_2). When Pt is deposited on the metal oxides, the bent band hinders the migration of most electrons from the MOF to the metal oxides and then to Pt, resulting in limited activity improvement.

Given the above results, MoO_3 and V_2O_5 can neither harvest visible light nor act as the cocatalyst or electron reservoirs in the MOF composites, as electrons are accumu-

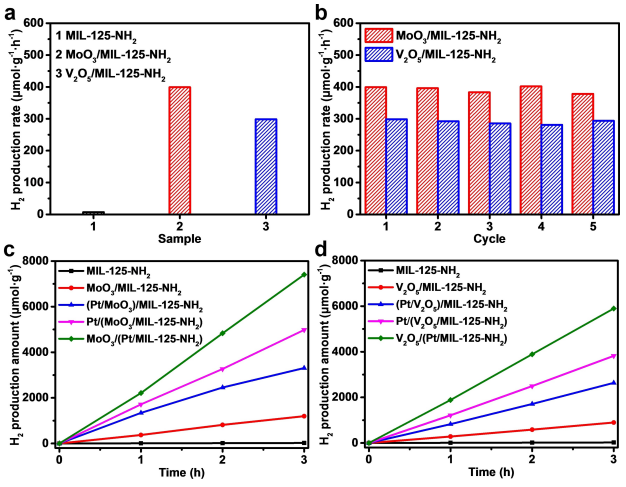

Figure 4. a) Photocatalytic H_2 production rates of MIL-125-NH_2, MoO_3/MIL-125-NH_2, and V_2O_5/MIL-125-NH_2. b) Recycling experiments of MoO_3/MIL-125-NH_2 and V_2O_5/MIL-125-NH_2. Photocatalytic H_2 production kinetic profiles of c) Pt-loaded MoO_3/MIL-125-NH_2 at different locations and d) Pt-loaded V_2O_5/MIL-125-NH_2 at different locations.

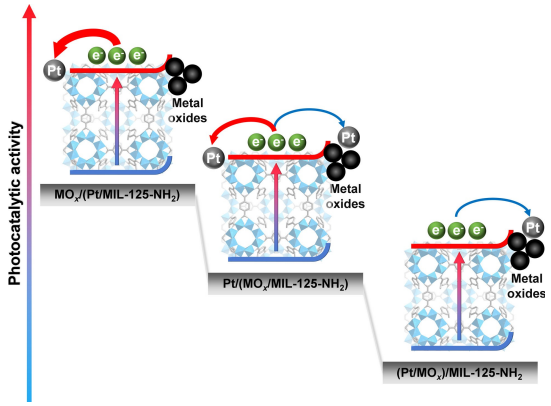

Scheme 3. Schematic diagrams of the Pt-deposited photocatalysts.

lated on the MOF. Accordingly, we are able to reach the mechanism of band bending induced by the integration of the metal oxides and the overall reaction details. Upon the MOF composite formation, the electrons on the HOMO of MIL-125-NH_2 would spontaneously migrate to the CB of the metal oxides due to the larger work functions of the latter (Scheme 2). When the equilibrium is achieved, the holes are accumulated on the HOMO of MIL-125-NH_2 and the upward band bending accordingly takes place. Given the uneven distribution of electrons and holes, the built-in electric field is formed at the near-surface of MIL-125-NH_2. On irradiation, the photogenerated electrons are driven by the built-in electric field to the MOF surface, following by the reaction with protons to generate H_2. On the other side, the photogenerated holes are driven to the interface, then react with the sacrificial agent triethylamine. Therefore, the effective separation of photogenerated carriers is achieved and the photocatalytic activity gets improved.

To further verify the mechanism proposed above, the photocatalytic H_2 production of diverse semiconductors with different band structures, including TiO_2, g-C_3N_4, and CdS, has been evaluated by the integration with the metal oxides under similar conditions. Under irradiation of UV/Vis light (>200 nm), the activities of both MoO_3/TiO_2 and V_2O_5/TiO_2 are even lower than that of TiO_2 (Figure S22a, b). On account of the higher CB of the metal oxides compared with the valence band (VB) of TiO_2, it is not possible for the electron transfer from the VB of TiO_2 to the CB of the metal oxides. Accordingly, the band bending and built-in electric field would not occur (Figure S22c). By contrast, the CB of MoO_3 is lower than the VB of g-C_3N_4 and CdS, which meets the requirement of the formation of upward band bending and built-in electric field. Similar to the MOF composites, under irradiation of visible light (>380 nm), the photocatalytic activities of the g-C_3N_4- and CdS-based composites are much enhanced in comparison with the single components (Figure S23, S24).

It should be noted that the band bending occurred to MoO_3/MIL-125-NH_2, and V_2O_5/MIL-125-NH_2 composites is distinctly different from the common heterojunction photocatalysts, which have been intensively reported (Figure S25):[21] 1) Both components in heterojunction photocatalysts can be photoexcited, while MoO_3 and V_2O_5 are hardly responsive to visible light (Figure S5). 2) The oxidation and reduction reactions take place on different components in heterojunction photocatalysts, while both oxidation and reduction reactions take place on MIL-125-NH_2 in the composites. These features demonstrate that MoO_3/MIL-125-NH_2 and V_2O_5/MIL-125-NH_2 do not follow the typical heterojunction mechanism. In addition, MoO_3 and V_2O_5 are neither active sites nor cocatalysts in photocatalysis, which can be concluded from the Pt-deposited control experiments (Figure 4c, d, S21) and the MoO_3/TiO_2 and V_2O_5/TiO_2 experiments (Figure S22a, b).

Conclusion

In summary, MIL-125-NH_2 is integrated with the metal oxides MoO_3 and V_2O_5. Their suited work functions and energy levels drive the electron transfer from the HOMO of the MOF to the CB of the metal oxides, giving rise to upward MOF band bending, and accordingly a built-in electric field at the near-surface of the MOF. In this case, though the metal oxides neither absorb photons nor accumulate electrons in the composites under visible light irradiation, the recombination of photogenerated carriers gets considerably suppressed, thereby regulating the charge properties of the MOF. As a consequence, the activity of MoO_3/MIL-125-NH_2 and V_2O_5/MIL-125-NH_2 dramatically increased by 56 and 42 times compared to the pristine MOF in photocatalytic H_2 production by water splitting under visible light irradiation. By further depositing Pt as cocatalyst on MIL-125-NH_2, around 6 times higher activity can be observed. This is the first report with clear evidence on band bending in MOFs, which is of great importance for not only rational fabrication but also better understanding of the mechanism in enhanced photocatalytic activity of MOF composites in the future, by taking advantage of the semiconductor-like behavior of MOFs.

Acknowledgements

This work was supported by the National Key Research and Development Program of China (2021YFA1500400), the National Natural Science Foundation of China (21725101, 22161142001, and 21871244), the DNL Cooperation Fund, Chinese Academy of Sciences (DNL201911), and Collaborative Innovation Program of Hefei Science Center, CAS (2020HSC-CIP005).

Conflict of Interest

The authors declare no conflict of interest.

Data Availability Statement

The data that support the findings of this study are available from the corresponding author upon reasonable request.

Keywords: Band Bending · Built-in Electric Field · Charge Separation · Metal–Organic Frameworks · Photocatalysis

[1] a) Q. Wang, K. Domen, *Chem. Rev.* **2020**, *120*, 919–985; b) J. Ran, J. Zhang, J. Yu, M. Jaroniec, S. Z. Qiao, *Chem. Soc. Rev.* **2014**, *43*, 7787–7812.

[2] a) X. Chen, S. Shen, L. Guo, S. S. Mao, *Chem. Rev.* **2010**, *110*, 6503–6570; b) H. Wang, L. Zhang, Z. Chen, J. Hu, S. Li, Z. Wang, J. Liu, X. Wang, *Chem. Soc. Rev.* **2014**, *43*, 5234–5244.

[3] a) G. Xu, H. Zhang, J. Wei, H.-X. Zhang, X. Wu, Y. Li, C. Li, J. Zhang, J. Ye, *ACS Nano* **2018**, *12*, 5333–5340; b) Y. Wang,

R. Godin, J. R. Durrant, J. Tang, *Angew. Chem. Int. Ed.* **2021**, *60*, 20811–20816; *Angew. Chem.* **2021**, *133*, 20979–20984.
[4] a) M. Zhang, M. Lu, Z.-L. Lang, J. Liu, M. Liu, J.-N. Chang, L.-Y. Li, L.-J. Shang, M. Wang, S.-L. Li, Y.-Q. Lan, *Angew. Chem. Int. Ed.* **2020**, *59*, 6500–6506; *Angew. Chem.* **2020**, *132*, 6562–6568; b) J. Bian, Z. Zhang, J. Feng, M. Thangamuthu, F. Yang, L. Sun, Z. Li, Y. Qu, D. Tang, Z. Lin, F. Bai, J. Tang, L. Jing, *Angew. Chem. Int. Ed.* **2021**, *60*, 20906–20914; *Angew. Chem.* **2021**, *133*, 21074–21082.
[5] a) K. Lan, R. Wang, Q. Wei, Y. Wang, A. Hong, P. Feng, D. Zhao, *Angew. Chem. Int. Ed.* **2020**, *59*, 17676–17683; *Angew. Chem.* **2020**, *132*, 17829–17836; b) X. Ma, L. Wang, Q. Zhang, H.-L. Jiang, *Angew. Chem. Int. Ed.* **2019**, *58*, 12175–12179; *Angew. Chem.* **2019**, *131*, 12303–12307.
[6] a) Q. Lin, X. Bu, C. Mao, X. Zhao, K. Sasan, P. Feng, *J. Am. Chem. Soc.* **2015**, *137*, 6184–6187; b) J.-D. Xiao, Q. Shang, Y. Xiong, Q. Zhang, Y. Luo, S.-H. Yu, H.-L. Jiang, *Angew. Chem. Int. Ed.* **2016**, *55*, 9389–9393; *Angew. Chem.* **2016**, *128*, 9535–9539; c) A. Indra, A. Acharjya, P. W. Menezes, C. Merschjann, D. Hollmann, M. Schwarze, M. Aktas, A. Friedrich, S. Lochbrunner, A. Thomas, M. Driess, *Angew. Chem. Int. Ed.* **2017**, *56*, 1653–1657; *Angew. Chem.* **2017**, *129*, 1675–1679; d) S. Kampouri, T. N. Nguyen, C. P. Ireland, B. Valizadeh, F. M. Ebrahim, G. Capano, D. Ongari, A. Mace, N. Guijarro, K. Sivula, A. Sienkiewicz, L. Forró, B. Smit, K. C. Stylianou, *J. Mater. Chem. A* **2018**, *6*, 2476–2481; e) T. N. Nguyen, S. Kampouri, B. Valizadeh, W. Luo, D. Ongari, O. M. Planes, A. Züttel, B. Smit, K. C. Stylianou, *ACS Appl. Mater. Interfaces* **2018**, *10*, 30035–30039; f) S. Kampouri, T. N. Nguyen, M. Spodaryk, R. G. Palgrave, A. Züttel, B. Smit, K. C. Stylianou, *Adv. Funct. Mater.* **2018**, *28*, 1806368.
[7] R. Chen, S. Pang, H. An, J. Zhu, S. Ye, Y. Gao, F. Fan, C. Li, *Nat. Energy* **2018**, *3*, 655–663.
[8] a) L. Peng, L. Hu, X. Fang, *Adv. Mater.* **2013**, *25*, 5321–5328; b) Z.-F. Huang, J. Song, X. Wang, L. Pan, K. Li, X. Zhang, L. Wang, J.-J. Zou, *Nano Energy* **2017**, *40*, 308–316; c) Z. Li, L. Zhang, Y. Liu, C. Shao, Y. Gao, F. Fan, J. Wang, J. Li, J. Yan, R. Li, C. Li, *Angew. Chem. Int. Ed.* **2020**, *59*, 935–942; *Angew. Chem.* **2020**, *132*, 945–952.
[9] X. Tao, Y. Gao, S. Wang, X. Wang, Y. Liu, Y. Zhao, F. Fan, M. Dupuis, R. Li, C. Li, *Adv. Energy Mater.* **2019**, *9*, 1803951.
[10] a) R. E. Morris, X. Bu, *Nat. Chem.* **2010**, *2*, 353–361; b) H. Furukawa, K. E. Cordova, M. O'Keeffe, O. M. Yaghi, *Science* **2013**, *341*, 1230444; c) B. Li, H.-M. Wen, Y. Cui, W. Zhou, G. Qian, B. Chen, *Adv. Mater.* **2016**, *28*, 8819–8860; d) T. Islamoglu, S. Goswami, Z. Li, A. J. Howarth, O. K. Farha, J. T. Hupp, *Acc. Chem. Res.* **2017**, *50*, 805–813; e) A. Dhakshinamoorthy, Z. Li, H. Garcia, *Chem. Soc. Rev.* **2018**, *47*, 8134–8172; f) J.-D. Xiao, H.-L. Jiang, *Acc. Chem. Res.* **2019**, *52*, 356–366; g) J. Nyakuchena, S. Ostresh, D. Streater, B. Pattengale, J. Neu, C. Fiankor, W. Hu, E. D. Kinigstein, J. Zhang, X. Zhang, C. A. Schmuttenmaer, J. Huang, *J. Am. Chem. Soc.* **2020**, *142*, 21050–21058.
[11] a) H. Liu, L. Chang, C. Bai, L. Chen, R. Luque, Y. Li, *Angew. Chem. Int. Ed.* **2016**, *55*, 5019–5023; *Angew. Chem.* **2016**, *128*, 5103–5107; b) H. Zhang, J. Wei, J. Dong, G. Liu, L. Shi, P. An, G. Zhao, J. Kong, X. Wang, X. Meng, J. Zhang, J. Ye, *Angew. Chem. Int. Ed.* **2016**, *55*, 14310–14314; *Angew. Chem.* **2016**, *128*, 14522–14526; c) Q. Yang, Q. Xu, H.-L. Jiang, *Chem. Soc. Rev.* **2017**, *46*, 4774–4808; d) G. Li, S. Zhao, Y. Zhang, Z. Tang, *Adv. Mater.* **2018**, *30*, 1800702; e) K. Sun, M. Liu, J. Pei, D. Li, C. Ding, K. Wu, H.-L. Jiang, *Angew. Chem. Int. Ed.* **2020**, *59*, 22749–22755; *Angew. Chem.* **2020**, *132*, 22937–22943.
[12] a) T. Zeng, D. Shi, Q. Cheng, G. Liao, H. Zhou, Z. Pan, *Environ. Sci. Nano* **2020**, *7*, 861–879; b) W. Cui, H. Bai, J. Shang, F. Wang, D. Xu, J. Ding, W. Fan, W. Shi, *Electrochim. Acta* **2020**, *349*, 136383.
[13] a) C. Wang, D. Liu, W. Lin, *J. Am. Chem. Soc.* **2013**, *135*, 13222–13234; b) J.-D. Xiao, L. Han, J. Luo, S.-H. Yu, H.-L. Jiang, *Angew. Chem. Int. Ed.* **2018**, *57*, 1103–1107; *Angew. Chem.* **2018**, *130*, 1115–1119; c) N. Kolobov, M. Goesten, J. Gascon, *Angew. Chem. Int. Ed.* **2021**, *60*, 26038–26052; *Angew. Chem.* **2021**, *133*, 26242–26256.
[14] a) Z. Li, J.-D. Xiao, H.-L. Jiang, *ACS Catal.* **2016**, *6*, 5359–5365; b) M. B. Chambers, X. Wang, L. Ellezam, O. Ersen, M. Fontecave, C. Sanchez, L. Rozes, C. Mellot-Draznieks, *J. Am. Chem. Soc.* **2017**, *139*, 8222–8228.
[15] a) M. Dan-Hardi, C. Serre, T. Frot, L. Rozes, G. Maurin, C. Sanchez, G. Férey, *J. Am. Chem. Soc.* **2009**, *131*, 10857–10859; b) T. Wang, X. Tao, Y. Xiao, G. Qiu, Y. Yang, B. Li, *Catal. Sci. Technol.* **2020**, *10*, 138–146.
[16] a) J. Meyer, S. Hamwi, M. Kröger, W. Kowalsky, T. Riedl, A. Kahn, *Adv. Mater.* **2012**, *24*, 5408–5427; b) I. A. de Castro, R. S. Datta, J. Z. Ou, A. Castellanos-Gomez, S. Sriram, T. Daeneke, K. Kalantar-zadeh, *Adv. Mater.* **2017**, *29*, 1701619.
[17] a) S. Porsgaard, P. Jiang, F. Borondics, S. Wendt, Z. Liu, H. Bluhm, F. Besenbacher, M. Salmeron, *Angew. Chem. Int. Ed.* **2011**, *50*, 2266–2269; *Angew. Chem.* **2011**, *123*, 2314–2317; b) Z. Zhang, J. T. Yates, *Chem. Rev.* **2012**, *112*, 5520–5551.
[18] R. Chen, F. Fan, T. Dittrich, C. Li, *Chem. Soc. Rev.* **2018**, *47*, 8238–8262.
[19] Y. Gao, W. Nie, X. Wang, F. Fan, C. Li, *Chem. Commun.* **2020**, *56*, 1007–1021.
[20] a) Y. Fu, D. Sun, Y. Chen, R. Huang, Z. Ding, X. Fu, Z. Li, *Angew. Chem. Int. Ed.* **2012**, *51*, 3364–3367; *Angew. Chem.* **2012**, *124*, 3420–3423; b) L. Shen, M. Luo, L. Huang, P. Feng, L. Wu, *Inorg. Chem.* **2015**, *54*, 1191–1193.
[21] a) C. Li, S. Dong, R. Tang, X. Ge, Z. Zhang, C. Wang, Y. Lu, L. Yin, *Energy Environ. Sci.* **2018**, *11*, 3201–3211; b) J. Wu, P. Huang, H. Fan, G. Wang, W. Liu, *ACS Appl. Mater. Interfaces* **2020**, *12*, 30304–30312; c) J. Wang, L. Xu, T. Wang, R. Li, Y. Zhang, J. Zhang, T. Peng, *Adv. Energy Mater.* **2021**, *11*, 2003575; d) C. Cheng, B. He, J. Fan, B. Cheng, S. Cao, J. Yu, *Adv. Mater.* **2021**, *33*, 2100317; e) J. Wang, E. Kim, D. P. Kumar, A. P. Rangappa, Y. Kim, Y. Zhang, T. K. Kim, *Angew. Chem. Int. Ed.* **2022**, *61*, e202113044; *Angew. Chem.* **2022**, *134*, e202113044; f) J. Wang, C.-S. Cao, J. Wang, Y. Zhang, L. Zhu, *Appl. Catal. B* **2022**, *304*, 121013.

Manuscript received: March 19, 2022
Accepted manuscript online: May 6, 2022
Version of record online: May 19, 2022